Effect of Time Window and Spectral Measurement Options on Empirical Green's Function Analysis Using DAS Array and Seismic Stations

Xiaowei Chen*[1], Jiuxun Yin[2], Colin Pennington[3], Qimin Wu[4], and Zhongwen Zhan[2]

ABSTRACT

The recorded seismic waveform is a convolution of event source term, path term, and station term. Removing high-frequency attenuation due to path effect is a challenging problem. Empirical Green's function (EGF) method uses nearly collocated small earthquakes to correct the path and station terms for larger events recorded at the same station. However, this method is subject to variability due to many factors. We focus on three events that were well recorded by the seismic network and a rapid response distributed acoustic sensing (DAS) array. Using a suite of high-quality EGF events, we assess the influence of time window, spectral measurement options, and types of data on the spectral ratio and relative source time function (RSTF) results. Increased number of tapers (from 2 to 16) tends to increase the measured corner frequency and reduce the source complexity. Extended long time window (e.g., 30 s) tends to produce larger variability of corner frequency. The multitaper algorithm that simultaneously optimizes both target and EGF spectra produces the most stable corner-frequency measurements. The stacked spectral ratio and RSTF from the DAS array are more stable than two nearby seismic stations, and are comparable to stacked results from the seismic network, suggesting that DAS array has strong potential in source characterization.

KEY POINTS

- Empirical Green's function (EGF) analysis is applied to three well-recorded earthquakes using a distributed acoustic sensing (DAS) array and seismic stations.
- A multitaper algorithm provides stable results of spectral fitting using the seismic network data.
- The DAS array data provide consistent and stable measurements of spectral complexity and the relative source time functions (RSTFs).

Supplemental Material

INTRODUCTION

The observed seismic waveform for an earthquake at a seismic station is the convolution of event source term ($e(t)$), path term ($p(t)$) and station term ($s(t)$):

$$d(t) = e(t) * p(t) * s(t). \quad (1)$$

The event source term at far field can be approximated as a source pulse with finite duration, and the integration of the source time function equals to the seismic moment. The source pulse can have varying durations at different azimuth due to directivity effect, with shorter duration in the rupture propagation direction. The spectrum of the source pulse is typically described as an Omega-square model, with a flat low-frequency part that scales with seismic moment, and a high-frequency fall-off rate above the corner frequency (Aki, 1967; Brune, 1970; Madariaga, 1976):

$$u(f) = \frac{\Omega_0}{(1 + (f/f_c)^{\gamma n})^{1/\gamma}}, \quad (2)$$

1. Department of Geology and Geophysics, Texas A&M University, College Station, Texas, U.S.A., https://orcid.org/0000-0001-6362-3297 (XC); 2. Seismological Laboratory, Division of Geological and Planetary Sciences, California Institute of Technology, Pasadena, California, U.S.A., https://orcid.org/0000-0003-0641-5680 (JY); https://orcid.org/0000-0002-5586-2607 (ZZ); 3. Lawrence Livermore National Laboratory, Livermore, California, U.S.A., https://orcid.org/0000-0002-1474-9368 (CP); 4. Lettis Consultants International, Inc., Concord, California, U.S.A., https://orcid.org/0000-0001-8315-8388 (QW)

*Corresponding author: xiaowei.chen@tamu.edu

Cite this article as Chen, X., J. Yin, C. Pennington, Q. Wu, and Z. Zhan (2025). Effect of Time Window and Spectral Measurement Options on Empirical Green's Function Analysis Using DAS Array and Seismic Stations, *Bull. Seismol. Soc. Am.* **XX**, 1–12, doi: 10.1785/0120240156

when $\gamma = 1$, $n = 2$, this is the "Brune" model (Brune, 1970), when $\gamma = 2$, $n = 2$, this is the "Boatwright" model (Boatwright, 1980). Generally, the influence of the source model on spectral fitting is relatively small (Abercrombie, 2015; Ruhl *et al.*, 2017; Bindi *et al.*, 2023; Cochran *et al.*, 2024; Lior, 2024).

Not all earthquakes can be well described with the simple theoretical source model with one corner frequency (equation 2). Uchide *et al.* (2014) found small earthquakes in Japan deviate from the simple source model. Such complex earthquakes have been widely found across different tectonic environments, for example, Parkfield (Abercrombie, 2014; Pennington *et al.*, 2022), southern California (Wu and Chen, 2018), earthquake swarms in Nevada (Ruhl *et al.*, 2017), and induced earthquakes in Oklahoma (Wu *et al.*, 2019). Source parameter estimations for complex earthquakes could have large variability (Abercrombie, 2014).

In addition to the complexity in source process, a major challenge is to correct path and site terms. Accurate high-frequency attenuation is often difficult to model with regional smoothed velocity models, and therefore, the empirical Green's function (EGF) method is developed. The nearly co-located small earthquake can be used to remove the path and site effects for a large earthquake recorded at the same station (Kane *et al.*, 2013). Theoretically, the small earthquake needs to be sufficiently small, so that it can be approximated as point source relative to the larger event. Time-domain implementation of the EGF method can be used to obtain the relative source time function (RSTF) of the larger event, examine directivity and slip distributions (e.g., López-Comino and Cesca, 2018; Wu *et al.*, 2019). Frequency-domain analysis can be used to obtain the spectral ratio between the two events, and perform model fitting to obtain the moment ratio, corner frequencies for the target and EGF events (e.g., Abercrombie, 2015; Huang *et al.*, 2017; Ruhl *et al.*, 2017). Note, some studies show that the magnitude difference requirement could be relaxed for spectral ratio analysis (e.g., Lior, 2024), which could facilitate studies in areas with narrow magnitude ranges.

The selection criteria for the EGF events have been extensively discussed in several studies (e.g., Kane *et al.*, 2013; Pennington *et al.*, 2023). The selection criteria range from simple distance-based selection, to selections considering focal mechanism similarities (Wu *et al.*, 2018), and correlation-based selection (Ruhl *et al.*, 2017). However, even using similar EGF selection criteria, the choice of bandwidth (Abercrombie, 2015), time window, wave type (Pennington *et al.*, 2021), and spectral measurement methods can lead to variations in the results (Chen *et al.*, 2024).

The Ridgecrest dataset provides an excellent opportunity for the community to further understand the causes of the source parameter measurement uncertainties by Baltay *et al.* (2024). Trugman (2020) and Bindi *et al.* (2023) conducted spectral analyses using large-scale generalized inversion approaches. Other studies focused on different aspects using this dataset. For example, Shearer *et al.* (2024) analyzed the impact of attenuation correction using two closely located earthquakes, Cochran *et al.* (2024) investigated the effects of inversion techniques, source model, and log- or linear sampling on spectral fitting using a set of benchmark spectra. Baltay *et al.* (2024) briefly summarized the community exercise in analyzing source parameters, and found wide range of variations among different studies. Chen *et al.* (2024) compared corner frequency and stress-drop results from spectral ratio and stacking approaches, and also found wide range of variations.

In this study, we focus on spectral ratio analysis to three well-recorded target earthquakes from the Ridgecrest stress-drop validation project (Baltay *et al.*, 2024). In addition to seismic stations from the Southern California Seismic Network (SCSN), the Ridgecrest sequence was also recorded by rapid response distributed acoustic sensing (DAS) arrays with existing fiber cables (Li *et al.*, 2021). The development of dense array observations has provided rich database for people to further quantify uncertainties and resolution of source processes (e.g., Fan and McGuire, 2018; Pennington *et al.*, 2023). The DAS arrays feature ultradense spatial resolution of ground-motion variations (Wang *et al.*, 2018; Zhan, 2019), and have been used for earthquake magnitude estimations (Yin *et al.*, 2023) and earthquake source processes (Li, Kim, *et al.*, 2023; Li, Zhu, *et al.*, 2023). Chen (2023) applied EGF analysis to two earthquakes recorded by collocated DAS and seismic nodal arrays, and found that the stacking power of DAS array produced smaller within-array uncertainty, and suggests that DAS has the potential in regular earthquake monitoring. Lior (2024) analyzed nine earthquakes using EGF method, and found DAS results to be more stable than the accelerometer network. A potential limitation of the DAS array is the "often" limited azimuthal coverage compared to regional seismic network.

For the three target earthquakes, we select EGF events that are well recorded by both the seismic network and the DAS array. We apply the same workflow to DAS and seismic datasets with varying time-window length and frequency bandwidth and compare the spectral ratio and RSTF results. We start with an examination of the effect of tapers and window length using different multitaper implementations. Then we examine different factors on the corner frequency and spectral residual measurements. Finally, we focus on example EGF event pairs to examine the stability of spectral ratio measurement and RSTF measured from DAS.

DATA

We first identify target events with $M \geq 3.5$ and potential EGF events (within 2 km hypocentral distance and at least one magnitude unit lower) from the data provided by the Ridgecrest stress-drop validation project from SCSN (Baltay *et al.*, 2024). Only seismic stations with sampling rates ≥100 Hz that record particle velocities are used in the analysis. Then we

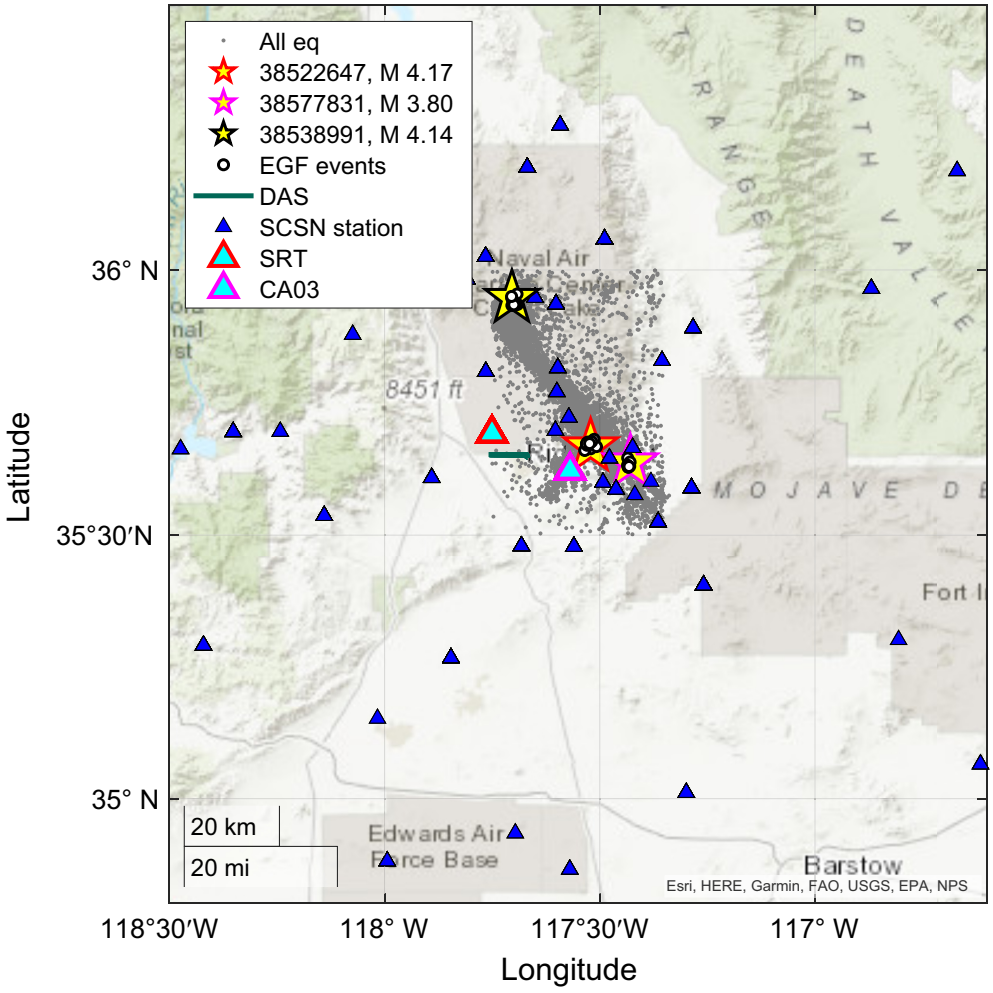

Figure 1. Map view of all available stations (blue triangle), two stations (cyan triangles, "SRT" and "CA03") closest to the distributed acoustic sensing (DAS) array (dark green line), all events in the Ridgecrest Validation project (gray dots) (Baltay *et al.*, 2024), the three target events (yellow stars), and their empirical Green's function (EGF) events (white circles). The color version of this figure is available only in the electronic edition.

extract the DAS waveform for each event from the rapid-response DAS array (resampled at 100 Hz) (Li *et al.*, 2021), which was deployed four days after the 2019 Ridgecrest mainshock. The array has a total length of 10 km, oriented in east–west direction, and has 1250 channels at 8 m spacing (Li *et al.*, 2021). A new machine learning phase picker based on transfer learning is applied to automatically pick *P* and *S* arrivals for cataloged events (Zhu *et al.*, 2023). We apply automated signal-to-noise assessment, followed by manual examination of the waveform to identify EGF events with high-quality waveform. We expand the stress-drop validation dataset to include later aftershocks from a relocated catalog (Hauksson *et al.*, 2012) to identify a larger number of suitable EGF events that have a high signal-to-noise ratio (SNR) from the DAS array. Three target events and 37 EGF events are identified (Fig. 1, Table S1, available in the supplemental material to this article), with 16 EGF events for target event 38522647 (**M** 4.17), 10 for target event 38577831 (**M** 3.8), and 11 for target event 38538991 (**M** 4.14).

Because DAS measures strain rate in the direction of the cable (Wang *et al.*, 2018), this east–west-oriented DAS array on the surface is more comparable to the east component of a seismometer. Therefore, we only consider the *S* wave in this study and compare DAS results with the east component from two nearby seismic stations ("SRT" and "CA03"), as well as results from all the available SCSN stations with only the east component ("SCSN-E") and both horizontal components ("SCSN-EN"), respectively. The example waveforms for three target events are shown in Figures S1–S3.

For plane-wave incidence, the strain measured from the DAS array can be related to particle velocity via the following equation: $\varepsilon = \pm \frac{1}{c}\dot{u}$ (in which ε,c,$\dot{u}$ are strain, wave velocity, and particle velocity, respectively) (Wang *et al.*, 2018). Lellouch *et al.* (2020) demonstrate that the raw DAS data can be used to measure relative microseismic event magnitudes, and Chen (2023) shows that EGF analysis applying to raw DAS data yields similar results with collocated geophones. Similar to Chen (2023), we directly use the raw DAS waveform for EGF analysis without any preprocessing.

METHOD

For each target earthquake, we use the same set of EGF events with the same selection criteria (SNR, variance reduction [VR]), and use the same set of spectral measurement methods and inversion algorithm.

We first perform a sensitivity test on the seismic network ("SCSN-EN", *S* wave measured as the geometric mean of the two horizontal components) using different spectral estimation methods with a continuous range of the number of tapers (2–16) and window length (3–30 s) to evaluate the variability of corner-frequency measurements due to spectral measurement methods and choices of taper and time window.

Then we select a limited set of parameters to examine the influence of dataset selection on spectral ratio and RSTF measurements. Specifically, we fix the number of tapers as 6, select four time windows (3, 5, 10, and 30 s), and four frequency bands with different low-frequency limits (0.2–25 Hz, 0.3–25 Hz, 0.8–25 Hz, and 1.5–25 Hz).

For "SCSN-EN", we only perform spectral ratio measurements. For "SCSN-E" (east component only), the two local stations ("CA03" and "SRT", east component only), and the DAS array (single-component channels oriented in east–west direction), we measure both spectral ratio and RSTF via deconvolution at each channel and compare both spectral ratio and RSTF results.

Multitaper methods

Multitaper spectral estimates typically reduce variance via averaging across multiple tapers (Prieto *et al.*, 2009). For those spectral estimates, a series of orthogonal discrete prolate spheroidal (Slepian) sequences is generated as window functions based on a "time-half-bandwidth (tbp)", and the number of tapers is typically calculated based on $2 * tbp - 1$ (Prieto *et al.*, 2009). The final spectrum is calculated based on the weighted average of modified spectra using these Slepian sequences (Thomson, 1982). In practice, the main difference between those different implementations is the weights of the modified spectra to calculate the average. We focus on two implementations: "pmtm" from MATLAB, and "mtspec" (for "SCSN-EN") and its variants ("mtdeconv" for single-component analysis: "SCSN-E", local stations, and DAS) from Prieto *et al.* (2009).

The "pmtm" (multitaper power spectral density estimate from MATLAB) uses the Thomson (1982) approach. The default "adapt" option is used, which uses frequency-dependent adaptive weighting to balance both the frequency concentration of the Slepian sequences and the power distribution in the time series.

The variants of the "mtspec" estimation method are from Prieto *et al.* (2009). This method estimates the power density spectrum using either a "Constant" multitaper that uses eigenvalue weights or an "Adaptive" multitaper that is similar to "pmtm" but a slightly different way of the iterative adaptive weighting calculation. Alternatively, the method also allows for a quadratic ("Quad") multitaper estimate (Prieto *et al.*, 2007), which uses a second derivative of the spectrum to obtain a higher resolution estimate of the spectrum.

In addition to the individual spectra measurement, we consider the "mtdeconv" approach (a variant of "mtspec"), which uses the "Adaptive" method to obtain optimal weights that simultaneously stabilize both the target and EGF event spectra and estimate RSTF via complex spectral division (Prieto *et al.*, 2009). The "mtdeconv" is the method adopted in Abercrombie (2015) to measure both spectral ratio and RSTF and investigate uncertainties.

Spectral ratio and RSTF measurement

For each event, the signal window starts at 0.1 s before the *S* arrival, and the noise window is a 3 s window that ends right before the *P* arrival. We keep the length of the noise window consistent, so we can focus on comparing relative changes in the signal spectra of different window lengths. All waveforms are zero-padded to 2048 samples for spectral measurements (Nfft = 2048). We only use spectra where both the target and EGF events have a minimum SNR greater than 2 within the desired frequency band (i.e., from the varied low-frequency limit to 25 Hz). For event pairs from the seismic network ("SCSN-EN" and "SCSN-E"), we require at least five stations to pass the SNR criteria. For the DAS array, we require at least 20 channels to meet the SNR criteria.

Using the spectra that passed the SNR criteria, we first average all available spectral ratios at individual stations for each pair, then perform spectral ratio fitting by obtaining moment ratio $M_0^R = \frac{M_0^{\text{Target}}}{M_0^{\text{EGF}[i]}}$ and corner frequencies for the target (f_c^{Target}) and EGF ($f_c^{\text{EGF}[i]}$) event from the Boatwright model (Pennington *et al.*, 2023):

$$R_i(f) = \frac{M_0^{\text{Target}}}{M_0^{\text{EGF}[i]}} \left[\frac{1 + (f/f_c^{\text{EGF}[i]})^4}{1 + (f/f_c^{\text{Target}})^4} \right]^{1/2}. \tag{3}$$

The spectral fitting is performed using the nonlinear solver from MATLAB ("fminsearch").

We only retain ratios with VR of the desired frequency bands greater than 70%. To obtain the VR, we first estimate the misfit between the median observed (obs) spectra across all common stations for a single (*i*th) EGF (R_i^{Obs}) and the predicted (R_i^{Syn}) ratio:

$$\text{Misfit}_i = [\log R_i^{\text{Obs}}(f) - \log R_i^{\text{Syn}} (f; M_0^{\text{Target}}/M_0^{\text{EGF}[i]}, f_c^{\text{Target}}, f_c^{\text{EGF}[i]})]^2, \tag{4}$$

and the VR is defined as

$$\text{VR}_i = \frac{\text{Misfit}_i}{\text{Var}(\log R_i^{\text{Obs}}(f))}, \tag{5}$$

in which "Var" denotes variance with respect to the logarithmic mean over the frequency band of interest.

After applying the VR criteria, we grid search for the "optimal" corner frequency for the target event that can simultaneously fit all EGF events while keep the corner frequencies for EGF events fixed at the best-fitting individual event pair fitting (Pennington *et al.*, 2023).

The RSTF is analyzed for selected individual target–EGF pairs to evaluate the influence of time window on RSTF stability. For the DAS array and SCSN-E stations (east component only) datasets, we use cross correlation to align RSTF from all available stations for each pair, then average all stations to get the final RSTF.

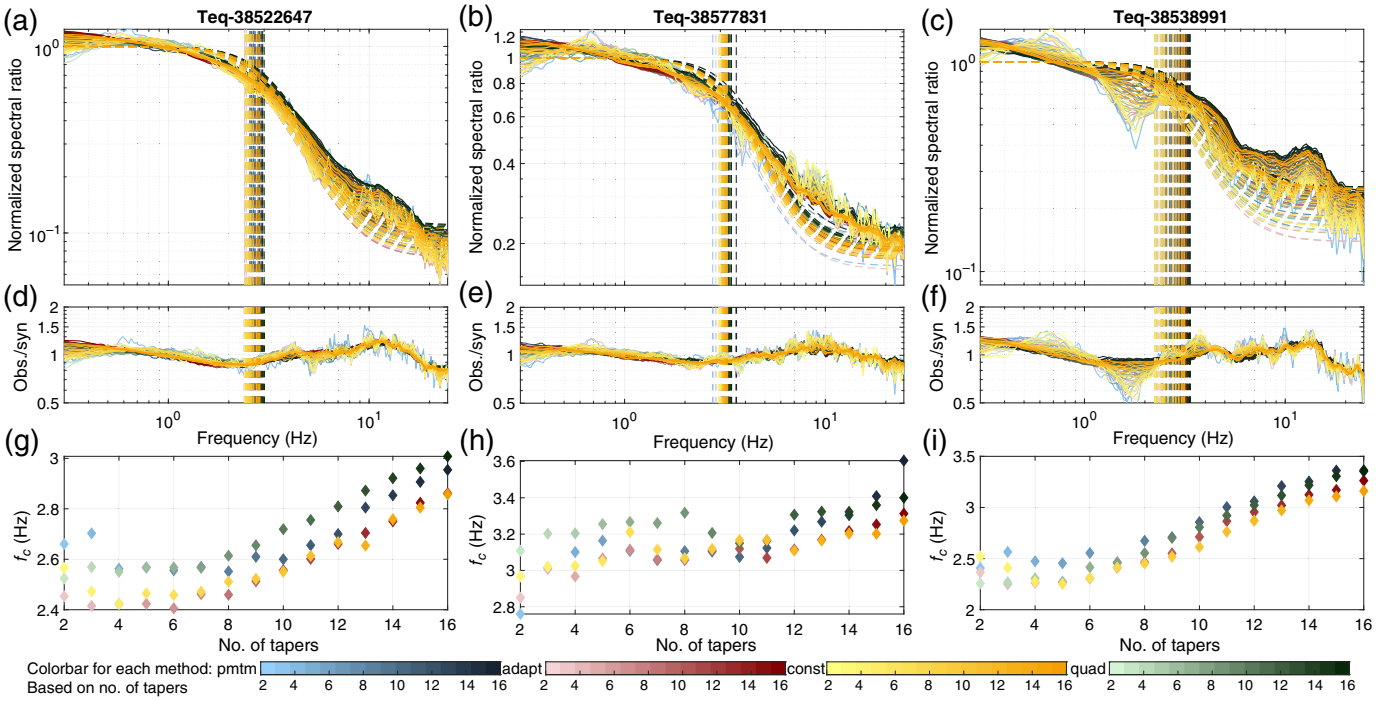

Figure 2. The effect of taper using different multitaper techniques on the three example events (a,d,g, event 38522647; b,e,h, event 38577831; c,f,i, event 38538991) using *S* wave from "SCSN-EN". For each event, the top panels (a, b, c) show the median spectral ratios of all EGF events as solid lines and synthetic fits as dashed lines. The vertical dashed line denotes the estimated corner frequency for each event. Each line is colored by their respective method and taper number (see color bars at the bottom of the figure). The middle panels (d, e, f) show the spectral residual from the median ratios to the synthetic curves. The bottom panels (g, h, i) show corner frequency as a function of the number of tapers. The color version of this figure is available only in the electronic edition.

EFFECT OF TAPERS AND SPECTRAL CALCULATION METHOD

We first examine the effect of the number of tapers and method of spectral calculation (Pennington *et al.*, 2022) for each target earthquake using the seismic network ("SCSN-EN"). For each pair of target and EGF events, we estimate their spectra using one of the aforementioned methods: "pmtm" from MATLAB, "mtspec" from Prieto *et al.* (2009) with "Constant," "Adaptive," or "Quad" options. For our tests, we only vary the method of estimation and number of tapers (*n*taper) from 2 to 16, and all other parameters are kept constant. The time-half-bandwidth product is calculated via (1 + *n*taper)/2. For each of these tests, we use 5 s *S*-wave window that starts 0.1 s before *S* arrival and fit the spectra from 0.3–25 Hz. Using a specified taper number and method, we estimate spectra for the target event and EGF events at each individual station and follow the workflow explained above to obtain an f_c from spectral ratio fitting (Pennington *et al.*, 2023). We only focus on the f_c of the target earthquake in this study, and a separate study to assess the uncertainties of the second f_c is underway (Abercrombie *et al.*, 2024).

The choice of method and number of tapers both affect the resulting spectra ratio (Fig. 2). For a fixed number of taper, the choice in method causes the estimated corner frequencies vary between methods by 0.1–0.4 Hz, with majority within 0.2 Hz of each other. The "Adaptive" and "Constant" methods generally produce lower estimated corner frequencies; whereas the "pmtm" and "Quad" methods tend to produce higher estimated corner frequencies.

For all methods, the corner frequencies tend to increase with the number of tapers, and the variability is larger than variability due to choice of methods (Fig. 2g–i). The increase in corner frequency with the number of tapers could be due to increase level of smoothing that reduce the prominence of troughs and peaks. This can be observed in the reduction of the spectral residual with more tapers in Figure 2d–f. For the complex event 38538991, significant smoothing of the "trough" between 1 and 2 Hz can be observed with larger number of tapers (Fig. 2f), and the corner frequency of this event increased from about 2.5 Hz with *n*taper = 7 to about 3.5 Hz with *n*taper = 15 (Fig. 2i).

For all three events, the corner frequencies are relatively stable with the number of tapers smaller than 6 or 7. Therefore, we fix the number of tapers as 6 (time-half-bandwidth product of 3.5) in the following analysis.

EFFECT OF TIME WINDOW AND SPECTRAL CALCULATION METHOD

We hold the number of tapers fixed as 6, frequency bandwidth as 0.3–25 Hz, and gradually change the *S*-wave window length from 3 to 30 s. We use the same dataset ("SCSN-EN") and the same set of spectral estimation methods.

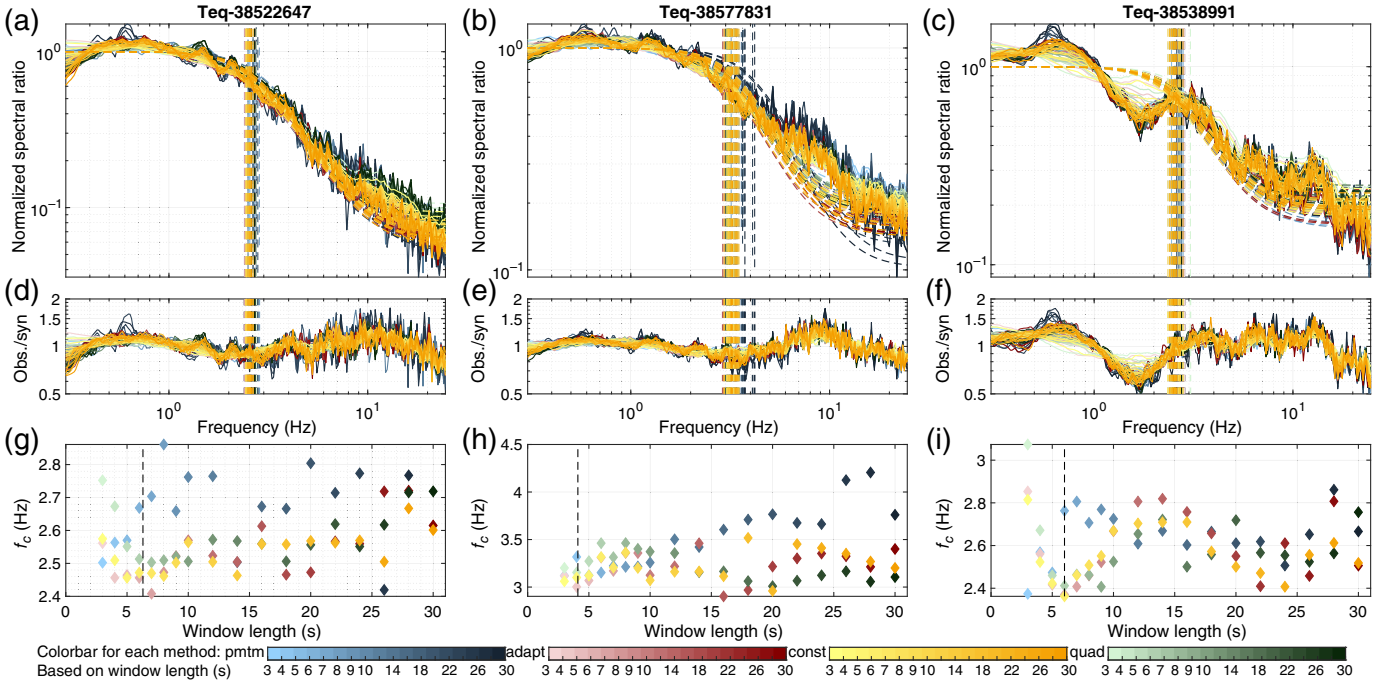

Figure 3. The effect of time window using different multitaper techniques on the three example events (a,d,g, event 38522647; b,e,h, event 38577831; c,f,i, event 38538991) using *S* wave from "SCSN-EN". For each event, the top panels (a, b, c) show the median spectral ratios of all EGF events as solid lines and synthetic fits as dashed lines. The vertical dashed line denotes the estimated corner frequency for each event. Each line is colored by their respective method and window length (see color bars at the bottom of the figure). The middle panels (d, e, f) show the spectral residual from the median ratios to the synthetic curves. The bottom panels (g, h, i) show corner frequency as a function of window length, and the vertical dashed line shows the reference time window calculated from equation (6). The color version of this figure is available only in the electronic edition.

Compared to the "mtspec" family of methods ("Adapt," "Constant," and "Quad"), the "pmtm" method appears more significantly influenced by the window length with much larger variability of corner frequencies and more outliers at longer window lengths (Fig. 3).

For "pmtm" method, the corner-frequency variation due to window length is larger than the number of tapers. For "mtspec" methods, the range of corner-frequency variations are similar; however, there is no clear relationship between corner frequency and window length (Fig. 3g–i, where corner frequency can increase or decrease with window length), which differs from the gradual increase of corner frequency with number of tapers (Fig. 2g–i).

For spectral ratio analysis, it is expected that the window length should be at least 10 times of the expected source duration, and Abercrombie *et al.* (2017) developed an equation to calculate time window based on the seismic moment of the target earthquake by assuming a constant stress drop of 0.1 MPa and *S* velocity of 4 km/s:

$$n\,\mathrm{sec} = \mathrm{round}\left(10 \times \frac{M_0^{1/3}}{20{,}000}\right)/10, \qquad (6)$$

in which M_0 is the seismic moment and "round" means rounding to nearest integer. This reference time window is plotted as vertical dashed lines in Figure 3g–i. For all three events, this reference time window falls within the range of window lengths where corner frequencies are relatively stable, suggesting that equation (6) is generally applicable in this study region.

Longer time windows tend to produce larger spectral deviations from the source model at low frequencies (Fig. 3d–f). This is likely due to the reduced SNR with increasing window length (Figs. S4–S6), leading to unconstrained moment ratio at low frequency, and hence larger variability of corner frequency (equation 3).

EFFECT OF DATASET SELECTION AND SPECTRAL MEASUREMENT OPTIONS

We now hold the number of taper fixed at 6, and apply limited selection of time window (3, 5, 10, and 30 s) and low-frequency limit (0.2, 0.3, 0.8, and 1.5 Hz) to the different datasets. We apply "mtspec" with "Adaptive" method and "pmtm" to "SCSN-EN" datasets. Moreover, we apply "mtdeconv" to "local" stations ("SRT" and "CA03" east component), "DAS" and available "SCSN-E" datasets, which allows measurements of both spectral ratio and RSTF. This produces 6 × 4 × 4 = 96 corner frequencies for each target event. We focus on a qualitative assessment of the "optimal" corner frequency and spectral deviation for each target earthquake from simultaneous fitting of multiple EGF events, as well as shapes of spectral ratio and RSTF from selected individual pairs

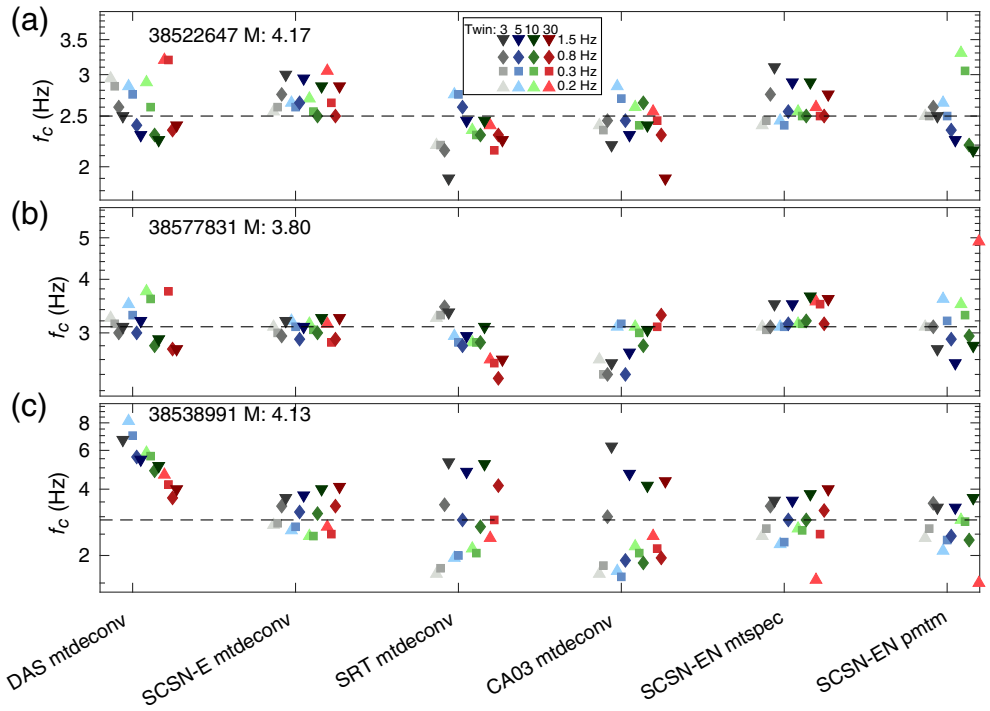

Figure 4. Best-fitting corner frequency for the three target earthquakes (a, event 38522647; b, event 38577831; c, event 38538991) for different datasets (indicated on the *X*-axis). The values are colored by their respective window length and low-frequency limit (see legend in panel a). To avoid overlapping symbols, these values are shifted from left to right by window length (short to long) and low-frequency limit (low to high). The horizontal dashed line indicates the median corner frequency for each event from all datasets. The color version of this figure is available only in the electronic edition.

(Pennington *et al.*, 2023). The results are summarized in Figures 4 and 5.

Figure 4 shows the "optimal" corner frequency for each target earthquake with different options, and Figure 5 shows the residual for the three target events separately, which can be used to identify complex (large residual with "bumps" and "troughs") or simple (small residual) earthquakes (Uchide and Imanishi, 2016).

1. Figure 4 shows that the variation of corner-frequency measurement is influenced by several factors:
   - Spectral measurement method: when using seismic network average ("SCSN-EN"), "pmtm" tends to produce more outliers than "mtspec", consistent with the time-window sensitivity test in Figure 3. Interestingly, we find that the "mtdeconv" algorithm produces the most stable results using the east component from all available seismic stations (SCSN-E). In "mtspec", each spectrum is individually calculated with different weights, whereas in "mtdeconv", the same weights are applied to calculate both target and EGF spectra. The more stable results from "mtdeconv" than "mtspec" suggest that the weights applied to multitaper spectral measurements could influence the spectral ratio results.
   - Frequency bandwidth: there is a general trend of increasing corner frequency with higher low-frequency limit using the network average, and such trend is more clearly observed for the complex event 38538991, where the estimated corner frequencies are above the median line with low-frequency limits of 0.8 and 1.5 Hz (Fig. 4c).
   - Window length: comparing the standard deviation for results using the same time window, we find that 5 s time window produces the lowest variability for the two simple events (38522647 and 38577831), whereas the 30 s produces largest variability. For the 5 s time window, 0.2 or 0.3 Hz low-frequency limit produces much lower variability compared to 0.8 or 1.5 Hz (Fig. 4). Measurements at individual stations ("SRT" and "CA03") are more sensitive to choices of window length compared to network average.
   - Overall, for the most well-constrained case "mtdeconv SCSN-E" using different time window and frequency bandwidth choices, the corner frequency varies within 0.15 Hz (one standard deviation) for the two simple events, and within 0.6 Hz for the more complex event 38538991.
2. Using "SCSN-EN" dataset, despite some differences in corner frequency between "pmtm" and "mtspec" methods, the spectral residuals are very consistent (Fig. 5). This is similar to observations in Chen *et al.* (2024), where two events have large variability in corner frequencies measured from different methods, but fairly consistent shape of spectral residual from model fitting. However, there is larger deviation at low frequency for longer time windows, especially for the 30 s window, this might explain the large variations of corner-frequency measurements using longer window and lower frequency.
3. Comparing the measurements between DAS and seismic data, we find that:
   - The DAS array tends to have comparable overall variability with individual stations (Fig. 4). For shorter time windows (3 and 5 s), the DAS results are more consistent

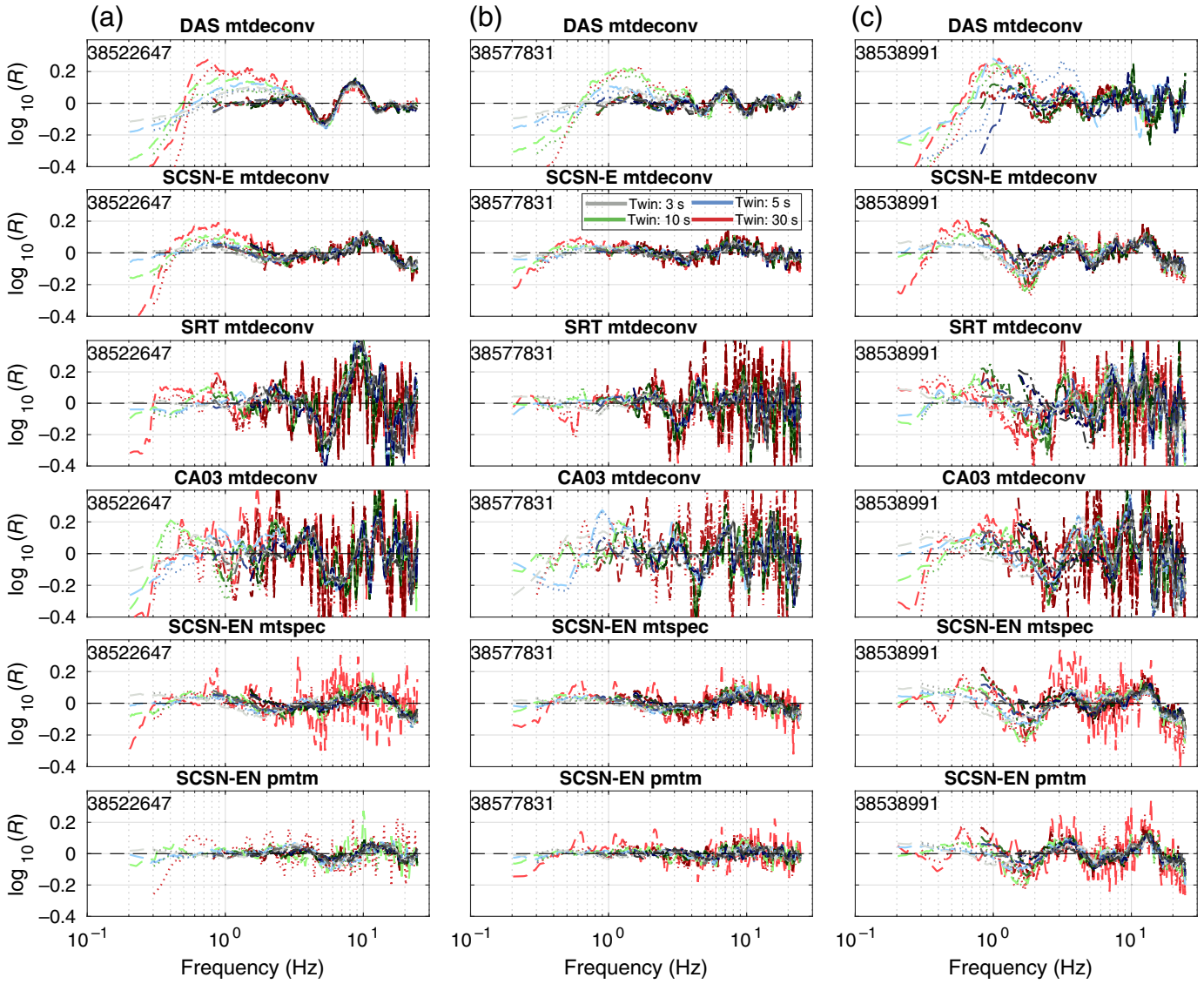

Figure 5. Spectral residual for all three target events (a, for 38522647; b, for 38577831; and c, for 38538991). Each subfigure corresponds to the dataset shown in Figure 4. Color groups indicate the time window: black for 3 s, blue for 5 s, green for 10 s, and red for 30 s. The line style and color gradients correspond to the low-frequency limit: 0.2 Hz (long dash: "–", light color), 0.3 Hz (":"), 0.8 Hz ("-."), and 1.5 Hz (solid line, dark color). The color version of this figure is available only in the electronic edition.

with the seismic network average for the two simple earthquakes (38522647 and 38577831). For the complex event 38538991, the DAS array results are systematically higher than the results from the seismic network, which is likely due to spectral complexity and large spectral residuals at low frequency (Fig. 5).

- At high frequency, the DAS array exhibits more stable spectral residual measurements for different time windows than the two nearby local stations ("SRT" and "CA03"), the difference is more clear for longer time windows (30 s), suggesting array measurement can effectively reduce uncorrelated noise.
- At low frequency, the DAS array exhibits larger spectral residual than the local stations and SCSN average (SCSN-E and SCSN-EN). This suggests that the sensitivity of DAS array at low frequency is likely lower compared to broadband seismic sensors. The SNRs on the DAS array for the three target events are generally lower than the seismic network (Figs. S7–S9).
- For event 38538991, the DAS array correctly identifies complex spectral residual that is similar to network average, but the two nearby local stations do not clearly show spectral complexity.
- For event 38522647, the spectral residuals from the DAS array and local stations ("SRT" and "CA03") are more complex than the network average using either SCSN-E or SCSN-EN. This could suggest some limitations due to limited azimuthal coverage for the DAS array.

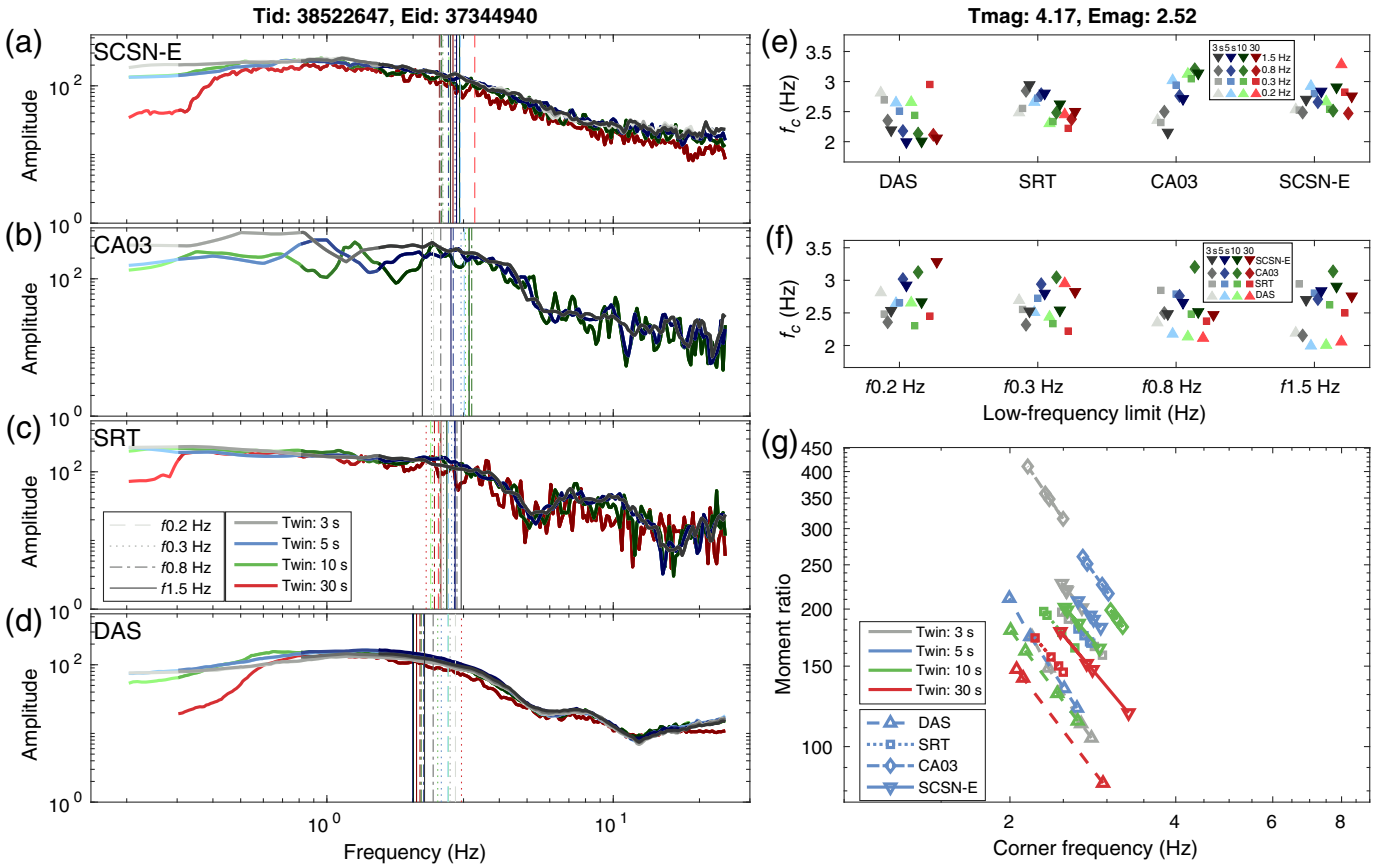

Figure 6. Example spectral ratio between target event 38522647 (**M** 4.17) and event 37344940 (**M** 2.52). For all figures, the colors of the (a–d, g) lines and (e,f) symbols correspond to the time window: black (3 s), blue (5 s), green (10 s), and red (30 s). (a) Averaged spectral ratio amplitude from the east component of all available stations. (b,c) Spectral ratio amplitudes from east component of "CA03" and "SRT" only. (d) Averaged spectral ratio amplitude from the DAS array. The vertical lines denote the best-fitting corner frequency for the target earthquakes. (a–d) Use the same line style that corresponds to the low-frequency limits (legend in panel c). (e) The corner frequency from different time windows and low-frequency limit for different datasets. The symbols correspond to low-frequency limits. (f) Similar to panel (e), the symbols correspond to different datasets, and the *x*-axis is the low-frequency limit. Values in panels (e) and (f) are shifted based on (e) window length and low-frequency limit or (f) dataset type to avoid overlapping. (g) The relationship between best-fitting moment ratio (*Y*-axis) and corner frequency (*x*-axis) for each pair for the same time window (indicated by color) and dataset (indicated by line style) using different frequency bandwidths. The color version of this figure is available only in the electronic edition.

The results shown here are based on average from multiple EGF events for the same target event. Because of the SNR and fitting criteria, different EGF events may be included with different datasets. For each target event, we compare the EGF events that have valid results from multiple datasets with different time window and low-frequency limit options to further examine shapes of spectral ratio and RSTF for individual pairs.

SPECTRAL RATIO AND RSTF FROM EXAMPLE EGF PAIRS

Figure 4 shows that the "mtdeconv" produces more stable results than "pmtm" and "mtspec" using SCSN network average, so we focus on the individual ratios from the "mtdeconv" method using four datasets, including DAS, SCSN-E, and two individual local stations. The spectral ratio and the corresponding RSTF for one example individual pair for event 38522647 are shown in Figures 6 and 7. Other example individual pair spectral ratios and RSTFs are included in Figures S10–S23 (in total, there are five examples for event 38522647, two for event 38577831, and one for 38538991).

Figure 6 shows that the low-frequency spectral ratio tends to dip downward with increasing time-window lengths, especially for the 30 s window. This is consistent with the larger spectral deviation at low frequency for longer windows in Figure 5 from averaging of multiple EGF events. Spectral ratios with longer time window also tend to have larger high-frequency noise, likely due to the reduced SNR for both target and EGF events at high frequency (Figs. S4–S6).

For measurements with the same time window and same dataset, but with different low-frequency limit, we find there exists strong trade-off between the moment ratio and target earthquake corner frequency (Fig. 6g), where higher moment ratio leads to lower corner frequency. The trade-off is more significant for the individual local stations than network average.

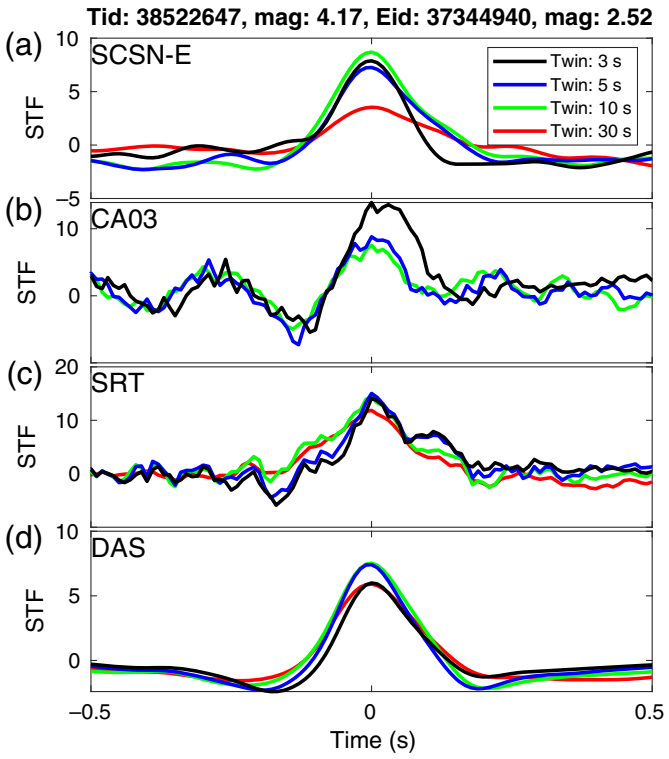

Figure 7. Example relative source time function (RSTF) between target event 38522647 (**M** 4.17) and event 37344940 (**M** 2.52). For all figures, the colors of the lines and symbols denote the time window: black (3 s), blue (5 s), green (10 s), and red (30 s). (a) Averaged from the east component of all available stations. (b,c) East component of "CA03" and "SRT" only. (d) The DAS array. The RSTFs are band-pass filtered between 0.1 and 10 Hz. The color version of this figure is available only in the electronic edition.

The seismic network average (SCSN-E) (Fig. 6a) has well-constrained flat spectral ratio at low frequency, extending all the way down to 0.2 Hz; however, the DAS ratio starts to decrease slightly below 1 Hz. This likely leads to the more significant trade-off between moment ratio and corner frequency for the DAS array for this pair. The trade-off between moment and corner frequency is also observed in Cochran *et al.* (2024) using a set of benchmark spectra.

The "mtdeconv" algorithm produces RSTF via complex spectral division (Abercrombie, 2015). For the DAS data, we find this method is preferred over time-domain methods developed for seismic data (e.g., Wu *et al.*, 2019). We originally applied the iterative forward modeling algorithm from Wu *et al.* (2019): this algorithm works well for seismic waveforms, but it produces very unstable RSTF using DAS data. Furthermore, although the spectral ratios from DAS tend to exhibit larger deviations at low frequency compared to seismic data (Fig. 5), the RSTF averaged from all usable DAS channels (e.g., those passed the SNR requirement) exhibits superior stability in spectral ratio and RSTF measurements compared to nearby local seismic stations. With a suitable EGF event, the RSTF exhibits comparable level of consistency to the seismic network average when using different time windows (Fig. 7). This is largely due to the stacking power of the DAS array, which usually is at least one order of magnitude denser than regular seismic network. The stability of DAS array-stacked RSTF is very encouraging, and suggests that the stacking power with high spatial sampling of the DAS array can effectively remove incoherent noise.

It should be noted that, not all EGF events are suitable for RSTF measurement. For example, event pair 38522647–38656095 has well-resolved spectral ratio and corner frequency, but the RSTF does not produce a clear pulse as other EGF events (Figs. S12 and S13), suggesting that RSTF inversion is more sensitive to EGF choices than spectral analysis (e.g., Abercrombie, 2015; Pennington *et al.*, 2023).

SUMMARY AND DISCUSSION

This study focuses on the *S* waves of three events that were well recorded by both the seismic network and the DAS array. By restricting the EGF pairs, the inversion method, we examine the effect of time window choices, frequency bandwidth, and spectral calculation options on averaged spectral ratio and individual event pairs.

Multitaper spectral estimates have been widely used in spectral analysis; however, different number of tapers and weighting algorithms could influence the spectral fitting results. A large number of tapers could cause higher estimated corner frequencies due to smoothing of spectral complexity. Although the differences due to algorithms are typically small, we find that the "pmtm" algorithm (from MATLAB) is more sensitive to window length and bandwidth choices (Figs. 3 and 4), and the method ("mtdeconv") (Prieto *et al.*, 2009) that use consistent weights for both the target and EGF events produce most stable results (Fig. 4). We recommend "mtdeconv" as a preferred method for EGF-based analysis, and a number of tapers smaller than 7 to avoid over smoothing.

For the DAS array, while the corner-frequency measurements exhibit larger scatter than the seismic network average (Fig. 4), the RSTFs obtained with suitable EGF events are generally more stable than individual seismic stations, and comparable to the average RSTF from seismic network for the simple earthquake (Fig. 7). This is largely due to the stacking power of the DAS array, which usually is at least one order of magnitude denser than regular seismic network. We recommend incorporating RSTF in DAS array-based source analysis.

Among the four different time windows, we find 5 s window produces lower variability, and most outliers are associated with the longest (30 s) time windows, with a few from the shortest (3 s) time windows (Fig. 4). This is consistent with the sensitivity test in Figure 3. Ideally, the time window should be at least a factor of 10 times the expected pulse duration of the target earthquake (Abercrombie *et al.*, 2017). The RSTF results show that the source duration for the three events range from 0.2 to 0.35 s, so 3 s is the minimum requirement of the

window length. For the two relatively simple events, the corner frequencies are stable for window lengths from 3 to 5 s (or 6 s) (Fig. 3). However, the corner frequencies for the complex event is more sensitive to shorter time windows. The window length calculated based on equation (6) generally agrees with the range of window length where corner frequencies are stable, and we recommend using this equation to guide future EGF analysis. Note that the time windows discussed here do not consider distance dependence, or coda waves.

A potential cause of the larger corner-frequency variability for longer time window (30 s) and the DAS array is due to the larger spectral deviation from source model at low frequencies (Fig. 6d), which could cause stronger trade-off between moment and corner frequency (Fig. 6g). We find that 0.3 Hz low-frequency limit tends to produce more consistent corner frequencies (Fig. 6f) than 0.8 and 1.5 Hz. Because the corner frequencies for each event is around 2–3 Hz, this implies that low-frequency limit should be at least a factor of 5–10 below the anticipated corner frequency. If independent moment estimates are available for both target and EGF events, fixing the moment ratios at low frequency could help mitigate this issue.

The event 83538991 has much larger variability than the other two events, this is possibly due to the spectral complexity (Fig. 5). The DAS array identified stable spectral residual measurements, which are very consistent with the average from SCSN seismic stations. However, measurements on the two nearby local stations are highly unstable and noisy. Based on the stable spectral complexity and RSTF measurement from the DAS array, we suggest that even though single DAS array may have limited azimuthal coverage, the stacking power from the high-resolution spatial sampling could provide robust characterization of earthquake source properties (e.g., Li, Kim, *et al.*, 2023).

DATA AND RESOURCES

The seismic and distributed acoustic sensing (DAS) data can be accessed through Amazon Web Services (AWS): https://scedc.caltech.edu/data/cloud.html (last accessed September 2022). MATLAB R2022a (www.mathworks.com/products/matlab, last access September 2024) is used to analyze data and generate all the figures in the manuscript. The software package GISMO (Thompson and Reyes, 2018) is used to organize waveform data. The supplemental material contains additional figures for individual target–empirical Green's function (EGF) pairs, a csv file with detailed event information, and a csv file with detailed corner-frequency results for different options shown in Figure 4.

DECLARATION OF COMPETING INTERESTS

The authors acknowledge that there are no conflicts of interest recorded.

ACKNOWLEDGMENTS

The authors thank the Southern California Earthquake Center (SCEC) for supporting the Ridgecrest stress-drop validation study. SCEC is funded by National Science Foundation (NSF) Cooperative Agreement EAR-1033462 and U.S. Geological Survey (USGS) Cooperative Agreement G12AC20038. This is SCEC Contribution 14152. Chen and Wu acknowledge support from SCEC Award 21169. Chen is also partially supported by SCEC Award 21032, 22042, and NSF Award 2328485. Colin Pennington's work was completed at Lawrence Livermore National Laboratory (LLNL) under Contract DE-AC52-07NA2734. The authors thank German Prieto for providing the MATLAB script for the multitaper algorithm ("mtspec" and "mtdeconv"). The authors thank editor Adrien Oth, reviewers Itzhak Lior, and Shanna Chu for detailed comments.

REFERENCES

Abercrombie, R. E. (2014). Stress drops of repeating earthquakes on the San Andreas fault at Parkfield, *Geophys. Res. Lett.* **41,** 8784–8791.

Abercrombie, R. E. (2015). Investigating uncertainties in empirical Green's function analysis of earthquake source parameters, *J. Geophys. Res.* **120,** 1–15.

Abercrombie, R. E., X. Chen, and Y. Huang (2024). How comparable are estimates of source parameters from the two earthquakes in a spectral ratio, and implications for source scaling, *AGU Fall Meeting*, Washington DC, USA.

Abercrombie, R. E., P. Poli, and S. Bannister (2017). Earthquake directivity, orientation, and stress drop within the subducting plate at the Hikurangi margin, New Zealand, *J. Geophys. Res.* **122,** 10,176–10,188.

Aki, K. (1967). Scaling law of seismic spectrum, *J. Geophys. Res.* **72,** 1217–1231.

Baltay, A., R. Abercrombie, S. Chu, and T. Taira (2024). The SCEC/USGS community stress drop validation study using the 2019 Ridgecrest earthquake sequence, *Seismica* **3,** doi: 10.26443/seismica.v3i1.1009.

Bindi, D., D. Spallarossa, M. Picozzi, A. Oth, P. Morasca, and K. Mayeda (2023). The community stress-drop validation study—part I: Source, propagation, and site decomposition of Fourier spectra, *Seismol. Res. Lett.* **94,** 1980–1991.

Boatwright, J. (1980). A spectral theory for circular seismic sources; simple estimates of source dimension, dynamic stress drop, and radiated seismic energy, *Bull. Seismol. Soc. Am.* **70,** 1–27.

Brune, J. N. (1970). Tectonic stress and the spectra of seismic shear waves from earthquakes, *J. Geophys. Res.* **75,** 4997–5009.

Chen, X. (2023). Source parameter analysis using distributed acoustic sensing – an example with the porotomo array, *Geophys. J. Int.* **233,** 2207–2213.

Chen, X., Q. Wu, and C. Pennington (2024). Influence factors of variability in stress drop measurements using stacking and spectral ratio methods for the Ridgecrest sequence, *Bull. Seismol. Soc. Am.* (in review).

Cochran, E. S., A. Baltay, S. Chu, R. E. Abercrombie, D. Bindi, X. Chen, G. A. Parker, C. Pennington, P. M. Shearer, and D. T. Trugman (2024). SCEC/USGS community stress drop validation study: How spectral fitting approaches influence measured source parameters, *Bull. Seismol. Soc. Am.* doi: 10.1785/0120240140.

Fan, W., and J. J. McGuire (2018). Investigating microearthquake finite source attributes with IRIS community wavefield demonstration experiment in Oklahoma, *Geophys. J. Int.* **214,** 1072–1087.

Hauksson, E., W. Yang, and P. M. Shearer (2012). Waveform relocated earthquake catalog for southern California (1981 to 2011), *Bull. Seismol. Soc. Am.* **102,** no. 5, 2239–2244.

Huang, Y., W. L. Ellsworth, and G. C. Beroza (2017). Stress drops of induced and tectonic earthquakes in the Central United States are indistinguishable, *Sci. Adv.* **3,** 1–8.

Kane, D. L., P. M. Shearer, B. P. Goertz-Allmann, and F. L. Vernon (2013). Rupture directivity of small earthquakes at Parkfield, *J. Geophys. Res.* **118,** 212–221.

Lellouch, A., R. Schultz, N. J. Lindsey, B. L. Biondi, and W. L. Ellsworth (2020). Low-magnitude seismicity with a downhole distributed acoustic sensing array—Examples from the FORGE geothermal experiment, *J. Geophys. Res.* **126,** e2020JB02046, doi: 10.1029/2020JB020462.

Li, J., T. Kim, N. Lapusta, E. Biondi, and Z. Zhan (2023). The break of earthquake asperities imaged by distributed acoustic sensing, *Nature* **620,** 800–806.

Li, J., W. Zhu, E. Biondi, and Z. Zhan (2023). Earthquake focal mechanisms with distributed acoustic sensing, *Nat. Commun.* **14,** doi: 10.1038/s41467-023-39639-3.

Li, Z., Z. Shen, Y. Yang, E. Williams, X. Wang, and Z. Zhan (2021). Rapid response to the 2019 Ridgecrest earthquake with distributed acoustic sensing, *AGU Adv.* **2,** e2021AV000395, doi: 10.1029/2021AV000395.

Lior, I. (2024). Accurate magnitude and stress drop using the spectral ratios method applied to distributed acoustic sensing, *Geophys. Res. Lett.* **51,** no. 1, doi: 10.1029/2023GL105153.

López-Comino, J. A., and S. Cesca (2018). Source complexity of an injection induced event: The 2016 mw5.1 Fairview, Oklahoma earthquake, *Geophys. Res. Lett.* **45,** 4025–4032.

Madariaga, R. (1976). Dynamics of an expanding circular fault, *Bull. Seismol. Soc. Am.* **66,** 639–666.

Pennington, C. N., H. Chang, J. L. Rubinstein, R. E. Abercrombie, N. Nakata, T. Uchide, and E. S. Cochran (2022). Quantifying the sensitivity of microearthquake slip inversions to station distribution using a dense nodal array, *Bull. Seismol. Soc. Am.* **112,** no. 3, 1252–1270.

Pennington, C. N., Q. Wu, X. Chen, and R. E. Abercrombie (2023). Quantifying rupture characteristics of microearthquakes in the Parkfield area using a high-resolution borehole network, *Geophys. J. Int.* **233,** 1772–1785.

Pennington, C. N., C. Xiaowei, R. Abercrombie, and W. Qimin (2021). Cross validation of stress drop estimates and interpretations for the 2011 Prague, OK, earthquake sequence using multiple methods, *J. Geophys. Res.* **126,** doi: 10.1029/2020JB020888.

Prieto, G. A., J. F. Lawrence, and G. C. Beroza (2009). Anelastic earth structure from the coherency of the ambient seismic field, *J. Geophys. Res.* **114,** doi: 10.1029/2008JB006067.

Prieto, G. A., R. L. Parker, D. J. Thomson, F. L. Vernon, and R. L. Graham (2007). Reducing the bias of multitaper spectrum estimates, *Geophys. J. Int.* **171,** 1269–1281.

Ruhl, C. J., R. E. Abercrombie, and K. D. Smith (2017). Spatiotemporal variation of stress drop during the 2008 Mogul, Nevada, earthquake swarm, *J. Geophys. Res.* **122,** doi: 10.1002/2017JB014601.

Shearer, P. M., I. Vandevert, W. Fan, R. E. Abercrombie, D. Bindi, G. Calderoni, X. Chen, W. Ellsworth, R. Harrington, Y. Huang, *et al.* (2024). Earthquake source spectra estimates vary widely for two Ridgecrest aftershocks because of differences in attenuation corrections, *Bull. Seismol. Soc. Am.* doi: 10.1785/0120240134.

Thomson, D. J. (1982). Spectrum estimation and harmonic analysis, *Proc. IEEE* **70,** 1055–1096.

Thompson, G., and C. Reyes (2018). GISMO - a seismic data analysis toolbox for MATLAB (Version 1.20b) [software], available at http://geoscience-community-codes.github.io/GISMO/ (last accessed February 2020), doi: 10.5281/zenodo.1404723.

Trugman, D. T. (2020). Stress-drop and source scaling of the 2019 Ridgecrest, California, earthquake sequence, *Bull. Seismol. Soc. Am.* **110,** 1859–1871.

Uchide, T., and K. Imanishi (2016). Small earthquakes deviate from the omega-square model as revealed by multiple spectral ratio analysis, *Bull. Seismol. Soc. Am.* **106,** doi: 10.1785/0120150322.

Uchide, T., P. Shearer, and K. Imanishi (2014). Stress drop variations among small earthquakes before the 2011 Tohoku-Oki Japan, earthquake and implications for the mainshock, *J. Geophys. Res.* **119,** doi: 10.1002/2014JB010943.

Wang, R., Y. J. Gu, R. Schultz, and Y. Chen (2018). Faults and non-double-couple components for induced earthquakes, *Geophys. Res. Lett.* **45,** 8966–8975.

Wu, Q., and X. Chen (2018). Characteristics of earthquake source complexity in the San Jacinto fault zone, *Poster Presentation at 2018 SCEC Annual Meeting*, available at https://southern.scec.org/publication/8653.

Wu, Q., M. C. Chapman, and X. Chen (2018). Stress drop variations of induced earthquakes in Oklahoma, *Bull. Seismol. Soc. Am.* **108,** 1107–1123.

Wu, Q., X. Chen, and R. Abercrombie (2019). Source complexity of the 2015 mw 4.0 Guthrie, Oklahoma earthquake, *Geophys. Res. Lett.* **46,** doi: 10.1029/2019GL082690.

Yin, J., W. Zhu, J. Li, E. Biondi, Y. Miao, Z. J. Spica, L. Viens, M. Shinohara, S. Ide, K. Mochizuki, *et al.* (2023). Earthquake magnitude with das: A transferable data-based scaling relation, *Geophys. Res. Lett.* **50,** doi: 10.1029/2023GL103045.

Zhan, Z. (2019). Distributed acoustic sensing turns fiber-optic cables into sensitive seismic antennas, *Seismol. Res. Lett.* **91,** 1–15.

Zhu, W., E. Biondi, J. Li, J. Yin, Z. E. Ross, and Z. Zhan (2023). Seismic arrival-time picking on distributed acoustic sensing data using semi-supervised learning, *Nat. Commun.* **14,** doi: 10.1038/s41467-023-43355-3.

Manuscript received 28 June 2024
Published online 4 March 2025